How the Cucumber Tendril Coils and Overwinds

Sharon J. Gerbode *et al.*

lack saprotrophic capability (1), CO_2 enhancement of AMF for N scavenging likely increases decomposition by stimulating (i.e., priming) saprotrophs in soil through three potential mechanisms. First, AMF likely grow preferentially toward (15), and thus facilitate saprotrophs' access to, new organic patches (24). Second, AMF slowly release labile C for saprotrophs at relatively low concentrations (3), likely engendering a larger priming effect on decomposition than roots (fig. S7) ($25–27$). And third, rapid removal of newly released NH_4^+ by AMF likely releases saprotrophs from metabolic repression (28).

Our findings indicate that CO_2 enhancement of AMF may alter terrestrial ecosystem C dynamics by stimulating decomposition of soil organic C in AMF-active zones. This effect will likely occur in its interplay with other controlling factors such as temperature and plant species composition (29). In many agro- or grassland ecosystems where AMF dominate (1), but no aboveground C pool with an annual incremental increase exists, CO_2 stimulation of AMF and organic C decomposition will mainly facilitate C turnover belowground, rather than ecosystem C sequestration (30). Even in forests with abundant AMF (e.g., tropical forests) (1), eCO$_2$ stimulation of AMF, although creating a transient C sink in plant biomass by facilitating N transfer from soil to plants and partially alleviating N limitation on plants (31), is likely to reduce the largest carbon stocks (soil C) in the system. Also, our results suggest that the form, rather than just the total amount, of soil N might play a major role in mediating belowground C turnover and plant N acquisition under eCO$_2$, thus offering a theoretical foundation for management of microbial N transformations in soil and plant N utilization to facilitate ecosystem C sequestration under future CO_2 scenarios.

References and Notes

1. S. E. Smith, D. J. Read, *Mycorrhizal Symbiosis* (Academic Press, San Diego, ed. 2, 2008).
2. E. T. Kiers *et al.*, *Science* **333**, 880 (2011).
3. B. Drigo *et al.*, *Proc. Natl. Acad. Sci. U.S.A.* **107**, 10938 (2010).
4. I. Jakobsen, L. Rosendahl, *New Phytol.* **115**, 77 (1990).
5. G. W. T. Wilson, C. W. Rice, M. C. Rillig, A. Springer, D. C. Hartnett, *Ecol. Lett.* **12**, 452 (2009).
6. J. M. Tisdall, S. E. Smith, P. Rengasamy, *Aust. J. Soil Res.* **35**, 55 (1997).
7. I. R. Sanders, R. Streitwolf-Engel, M. G. A. van der Heijden, T. Boller, A. Wiemken, *Oecologia* **117**, 496 (1998).
8. K. K. Treseder, M. F. Allen, *New Phytol.* **147**, 189 (2000).
9. O. Alberton, T. W. Kuyper, A. Gorissen, *New Phytol.* **167**, 859 (2005).
10. M. C. Rillig, S. F. Wright, M. F. Allen, C. B. Field, *Nature* **400**, 628 (1999).
11. S. Hu, F. S. Chapin III, M. K. Firestone, C. B. Field, N. R. Chiariello, *Nature* **409**, 188 (2001).
12. K. H. Orwin, M. U. F. Kirschbaum, M. G. St John, I. A. Dickie, *Ecol. Lett.* **14**, 493 (2011).
13. A. Hodge, A. H. Fitter, *Proc. Natl. Acad. Sci. U.S.A.* **107**, 13754 (2010).
14. C. Tu *et al.*, *Glob. Change Biol.* **12**, 793 (2006).
15. A. Hodge, C. D. Campbell, A. H. Fitter, *Nature* **413**, 297 (2001).
16. See supplementary materials on *Science* Online.
17. S. Solomon *et al.*, *Climate Change 2007: The Physical Science Basis Contribution of Working Group I to the Fourth Assessment Report of the Intergovernmental Panel on Climate Change* (Cambridge Univ. Press, Cambridge, 2007).
18. L. Cheng *et al.*, *PLoS ONE* **6**, e21377 (2011).
19. A. J. Bloom, M. Burger, J. S. R. Asensio, A. B. Cousins, *Science* **328**, 899 (2010).
20. A. J. Bloom, D. R. Smart, D. T. Nguyen, P. S. Searles, *Proc. Natl. Acad. Sci. U.S.A.* **99**, 1730 (2002).
21. H. J. Di *et al.*, *Nat. Geosci.* **2**, 621 (2009).
22. C. R. Fellbaum *et al.*, *Proc. Natl. Acad. Sci. U.S.A.* **109**, 2666 (2012).
23. M. Govindarajulu *et al.*, *Nature* **435**, 819 (2005).
24. P. Bonfante, I.-A. Anca, *Annu. Rev. Microbiol.* **63**, 363 (2009).
25. R. P. Phillips, A. C. Finzi, E. S. Bernhardt, *Ecol. Lett.* **14**, 187 (2011).
26. K. M. Carney, B. A. Hungate, B. G. Drake, J. P. Megonigal, *Proc. Natl. Acad. Sci. U.S.A.* **104**, 4990 (2007).
27. M.-A. de Graaff, A. T. Classen, H. F. Castro, C. W. Schadt, *New Phytol.* **188**, 1055 (2010).
28. D. Geisseler, W. R. Horwath, R. G. Joergensen, B. Ludwig, *Soil Biol. Biochem.* **42**, 2058 (2010).
29. E. A. Davidson, I. A. Janssens, *Nature* **440**, 165 (2006).
30. K. J. van Groenigen, C. W. Osenberg, B. A. Hungate, *Nature* **475**, 214 (2011).
31. P. B. Reich *et al.*, *Nature* **440**, 922 (2006).

How the Cucumber Tendril Coils and Overwinds

Sharon J. Gerbode,[1,2,3]* Joshua R. Puzey,[4]* Andrew G. McCormick,[5] L. Mahadevan[1,2,4,5]†

The helical coiling of plant tendrils has fascinated scientists for centuries, yet the underlying mechanism remains elusive. Moreover, despite Darwin's widely accepted interpretation of coiled tendrils as soft springs, their mechanical behavior remains unknown. Our experiments on cucumber tendrils demonstrate that tendril coiling occurs via asymmetric contraction of an internal fiber ribbon of specialized cells. Under tension, both extracted fiber ribbons and old tendrils exhibit twistless overwinding rather than unwinding, with an initially soft response followed by strong strain-stiffening at large extensions. We explain this behavior using physical models of prestrained rubber strips, geometric arguments, and mathematical models of elastic filaments. Collectively, our study illuminates the origin of tendril coiling, quantifies Darwin's original proposal, and suggests designs for biomimetic twistless springs with tunable mechanical responses.

The transformation of a straight plant tendril into a helically coiled shape has inspired numerous studies since the 1800s (*1–8*), both from mechanistic and functional perspectives. Tendrils serve climbing plants by providing a parasitic alternative to building independently stable structural supports, allowing the plant to wend its way to sunlight and numerous ecological niches (*9*). During climbing, an initially straight tendril first finds and attaches to a support (fig. S1 and movie S1). Once tethered, the tendril coils by forming two oppositely handed helices connected by a "perversion" (Fig. 1, A and B), which was recognized by Darwin as a topological necessity given the clamped boundary conditions at each end of the tendril (*3*). This helical coiling axially shortens the tendril, hoisting the plant toward the attachment point (fig. S1 and movie S1).

Despite the long history of studying tendrils, the basic mechanism of tendril coiling has remained elusive. Historically, experimental studies of diverse tissues [reaction wood (*10*), hypocotyls (*11*), twining stems (*12, 13*), and leaves (*14*)] have addressed aspects of curvature generation, whereas

[1]School of Engineering and Applied Sciences, Harvard University, Cambridge, MA 02138, USA. [2]Wyss Institute for Biologically Inspired Engineering, Harvard University, Cambridge, MA 02138, USA. [3]Department of Physics, Harvey Mudd College, Claremont, CA 91711, USA. [4]Department of Organismic and Evolutionary Biology, Harvard University, Cambridge, MA 02138, USA. [5]Department of Physics, Harvard University, Cambridge, MA 02138, USA.

*These authors contributed equally to this work.
†To whom correspondence should be addressed. E-mail: lm@seas.harvard.edu.

theoretical treatments have incorporated intrinsic curvature or differential growth without addressing its origin or mechanical consequences (*6*, *15*, *16*). Recent studies of tendril anatomy (*17*, *18*) have provided a new twist by revealing an interior layer of specialized cells similar to the stiff, lignified gelatinous fiber (g-fiber) cells found in reaction wood (*19*). These cells provide structural support in reaction wood via tissue morphosis driven by cell-wall lignification, water flux, and oriented stiff cellulose microfibrils. The presence of a similar ribbon-like strip of g-fiber cells in tendrils suggests that the coiling of the soft tendril tissue may be driven by the shaping of this stiff, internal "fiber ribbon" (*18*).

We investigated the role of the fiber ribbon during tendril coiling in both *Cucumis sativus* (cucumber) and *Echinocystis lobata* (wild cucumber) (*20*). The g-fiber cells, identified in wild cucumber by using xylan antibodies in (*18*), are easily distinguished as a band of morphologically differentiated cells consistently positioned along the inner side of the helical tendril that lignify during coiling (*17*, *18*). In straight tendrils that have not yet attached to a support (Fig. 1A), a faint band of immature g-fiber cells is barely visible by using darkfield microscopy (Fig. 1B), with no ultraviolet (UV) illumination signature, indicating the absence of lignification (Fig. 1C). In coiled tendrils (Fig. 1D), g-fiber cells are clearly visible (Fig. 1E) and lignified (Fig. 1F). The fiber ribbon consists of two cell layers, with the ventral layer

on the inside of the helix showing increased lignification relative to the dorsal outer layer (Fig. 1, G and H), which is consistent with earlier observations of increased lignification on the stimulated side of the tendril (*17*, *18*). When a fiber ribbon is extracted from the coiled tendril by using fungal carbohydrolases [Driselase (Sigma-Aldrich, St. Louis, MO)] to break down the nonlignified epidermal tendril tissue (*20*), it retains the helical morphology of a coiled tendril, and furthermore, lengthwise cuts do not change its shape (Fig. 1I and fig. S2).

These observations suggest that tendril coiling occurs via asymmetric contraction of the fiber ribbon; the ventral side shrinks longitudinally relative to the dorsal side, giving the fiber ribbon its intrinsic curvature. The asymmetric contraction may be generated by a variety of dorsiventral asymmetries, including the observed differential lignification (Fig. 1H), variations in cellulose microfibril orientation as in reaction wood, or differential water affinities. For example, because lignin is hydrophobic the ventral cells may expel more water during lignification, driving increased cell contraction. This would be consistent with observations of extracted fiber ribbons that passively shrink and coil even further when dried but regain their original shape when rehydrated (movie S2). Dehydrated tendrils also exhibit this behavior because they are dominated by the stiff fiber ribbon (movie S3). Together, these facts suggest that the biophysical mechanism for

tendril coiling is provided by the asymmetric contraction of the stiff fiber ribbon, whose resulting curvature is imposed on the surrounding soft tendril tissue. The perversions in a doubly supported tendril follow naturally from the topological constraint imposed by the prevention of twist at its ends.

To better understand the origin of curvature in fiber ribbons, we reconstituted the underlying mechanism using a physical model composed of two bonded, differentially prestrained silicone rubber sheets, similar to rubber models for shaping sheets (*21*–*23*). The first silicone sheet was uniaxially stretched, and an equally thick layer of silicone sealant was spread onto the stretched sheet. After the sealant was fully cured, thin strips were cut along the prestrained direction, yielding bilayer ribbons (Fig. 2A) with intrinsic curvature set by the relative prestrain, thickness, and stiffness of the two layers (fig. S3) (*20*). Like fiber ribbons, the initially straight physical models spontaneously form coiled configurations with two opposite-handed helices connected by a helical perversion (Fig. 2A, left).

However, there is an unexpected difference in mechanical behavior between the physical models and tendril fiber ribbons. When clamped at both ends and pulled axially, the physical model simply unwinds to its original uncoiled state (Fig. 2A and movie S4). In contrast, in fiber ribbons we observed a counterintuitive "overwinding" behavior in which the ribbon coils even further
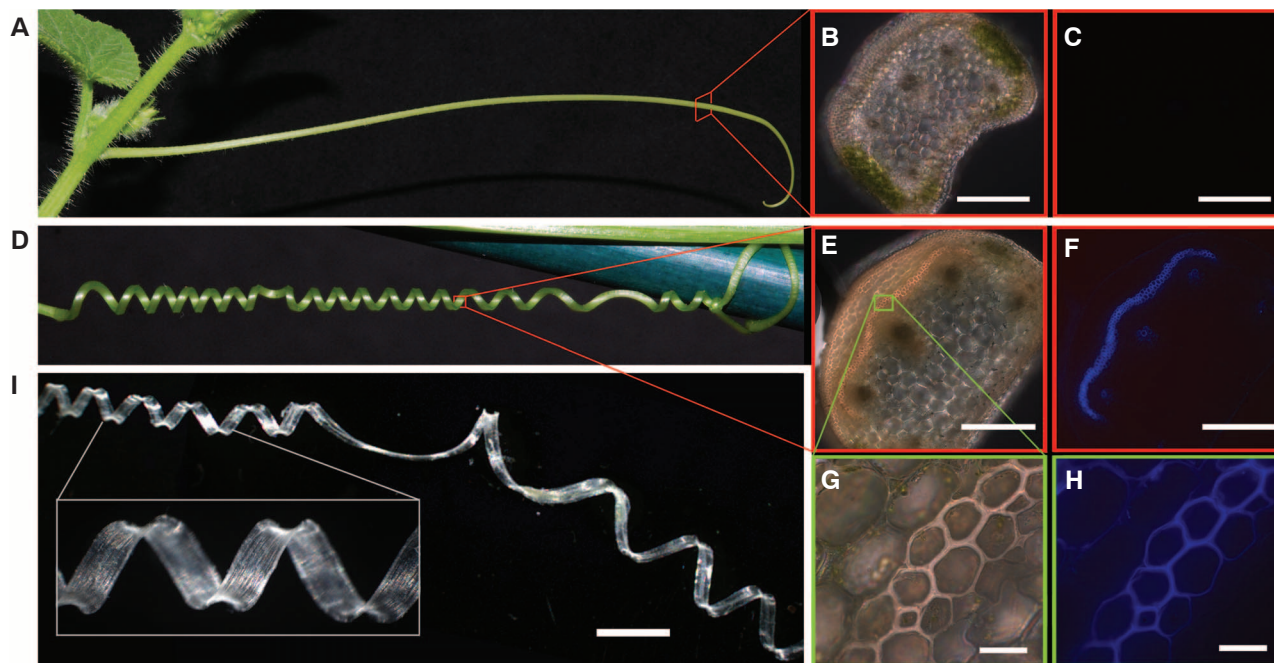
Fig. 1. Tendril coiling via asymmetric contraction. During coiling, a strip of specialized structural gelatinous fiber cells (the fiber ribbon) becomes lignified and contracts asymmetrically and longitudinally. (**A** to **C**) A straight tendril that has never coiled (A) lacks lignified g-fiber cells. In the tendril cross section, darkfield (B) and UV autofluorescence (C) show no lignin signal. (**D** to **H**) In coiled tendrils (D), the fully developed fiber ribbon consists of ~2 layers of highly lignified cells extending along the length of the tendril. In the tendril cross section, darkfield (E) and UV autofluorescence (F) show strong lignification in the fiber ribbon. In (G) and (H), increased magnification reveals that ventral cells (top left) are more lignified than dorsal cells. (**I**) The extracted fiber ribbon retains the helical morphology of the coiled tendril. (Inset) Higher magnification shows the orientation of g-fiber cells along the fiber ribbon. Scale bars, (B) and (C) 0.5 mm, (E) and (F) 100 μm, (G) and (H) 10 μm, (I) 1 mm.

when pulled, adding turns on both sides of the perversion (Fig. 2A, right, and movie S5). Eventually though, under high enough tension the fiber ribbon unwinds, returning to a flat, uncoiled state as expected (movie S5).

Inspired by our observations of asymmetric lignification in fiber ribbons, which suggest that the inner layer is less extensible, we added a relatively inextensible fabric ribbon to the inside of a coiled physical model. To mimic lignified cells that resist compression, we added an incompressible copper wire to the exterior of the helix. The internal fabric ribbon prevents elongation, whereas the external copper wire prevents contraction. Together, these modifications increase
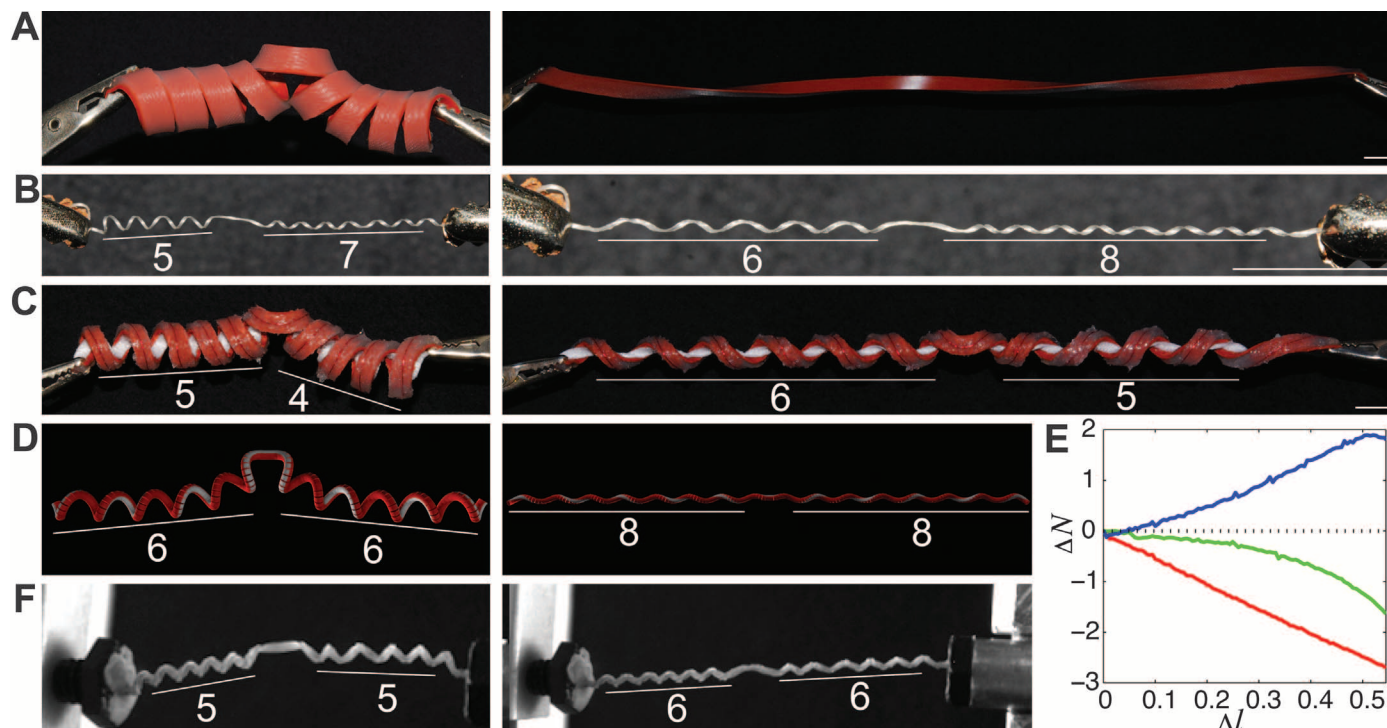
**Fig. 2. Twistless springs unwinding and overwinding. (A)** A silicone twistless spring with lower bending stiffness B than twisting stiffness C unwinds when pulled, returning to its original flat shape. **(B)** When a fiber ribbon is pulled, it initially overwinds, adding one extra turn to each side of the perversion (number of turns are indicated in white). **(C)** Overwinding is induced in the silicone model by adding a relatively inextensible (under tension) fabric ribbon to the interior of the helix and an inextensible (under compression) copper wire to the exterior. Together, these increase the ratio B/C. **(D)** When $B/C > 1$, numerical simulations of elastic helical filaments recapitulate this overwinding behavior, which is consistent with physical and biological experiments. **(E)** Change in the number of turns in each helix ΔN is plotted versus scaled displacement Δl for B/C values 1/5 (red), 1 (green), and 5 (blue). Overwinding becomes more pronounced with increasing B/C. **(F)** Overwinding is also observed in old tendrils, which have dried and flattened into a ribbon-like shape with $B/C > 1$. Scale bars, 1 cm.

Fig. 3. Mechanical consequences of overwinding. **(A** and **B)** Force extension curves for one young tendril that does not overwind (red curves) and one old tendril that exhibits substantial overwinding (blue curves). Each tendril was separated into a segment containing the helical perversion (dotted curves indicate perverted) and a segment with no perversion (solid curves indicate clamped). The dimensionless force $\tilde{F}$ is plotted against the scaled displacement Δl (detailed definitions are available in the supplementary materials) in (A). The difference in scaled force due to the helical perversion $\Delta f = f(\text{perverted}) - f(\text{clamped})$ is plotted against Δl in (B). The shaded range in (B) indicates variations in the fitted initial slope value. **(C)** Dimensionless force-extension curves are plotted for numerical filaments with B/C values 1/5 (red), 1 (green), 5 (blue). (Inset) Log-linear plot of the same data. **(D)** The difference in force $\Delta \tilde{F} = \tilde{F}(\text{perverted}) - \tilde{F}(\text{clamped})$ highlights the mechanical effect of the helical perversion. For $B < C$, the perversion always decreases the force needed to axially extend the filament; for $B > C$, the perversion initially decreases the force needed but eventually increases this necessary force at higher extensions. (Inset) Δf is plotted against Δl for direct comparison with the experimental data.
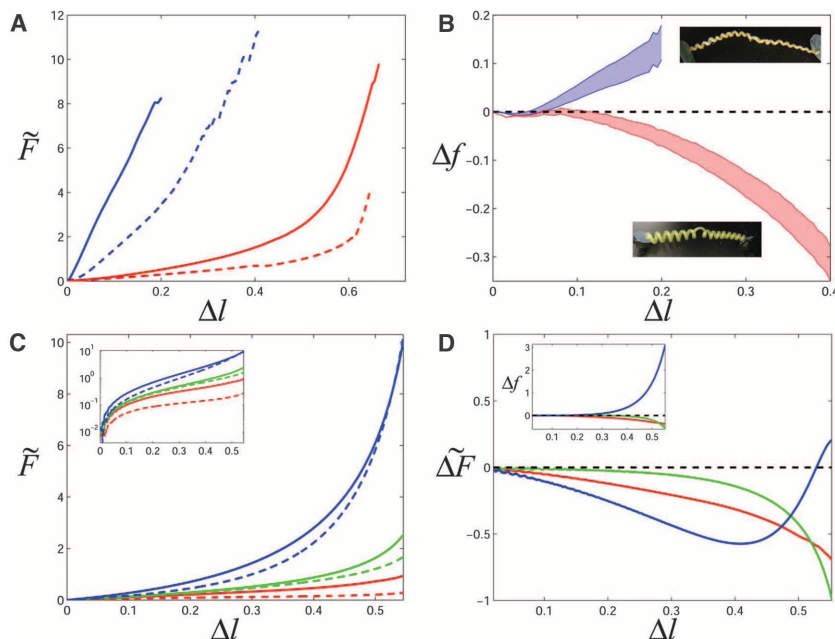
the model's effective bending stiffness relative to its twisting stiffness, fixing its intrinsic helix curvature while still allowing twist about its centerline (20). The modified model exhibited substantial overwinding (Fig. 2C and movie S6). Indeed, a single helix with infinite bending stiffness and fixed curvature cannot extend without its ends rotating. However, if one end may rotate, additional axial length can be accommodated by changing both pitch and radius to maintain constant curvature, resulting in additional helical turns (20). The perversion connecting helices of opposite handedness allows rotation and enables the addition of helical turns. By overwinding, each helix can thus geometrically accommodate axial extension without varying its curvature (fig. S4).

Of course, real tendril fiber ribbons have finite stretching and bending stiffness, and eventually at sufficiently high tensions, the helices unwind. To study overwinding in a fiber ribbon with finite bending and twisting stiffness, we modeled it mathematically as a filament composed of two equal-length, elastic helices of opposite handedness but identical intrinsic curvature k_0 and torsion w_0, and uniform bending stiffness B and twisting stiffness C, connected by a single helical perversion (Fig. 2D, left). When the filament, initially at equilibrium, is pulled apart at its clamped ends, deviations from equilibrium values of curvature and twist lead to variations in the filament's total energy (20). Minimizing the energy of the extended filament numerically (20), we determined the filament shape and position as a function of the applied tension (Fig. 2D, right). When $B/C < 1$, the filament unwinds on extension, but when $B/C > 1$, the filament overwinds (Fig. 2D and movies S7 and S8), and the number of additional turns ΔN increases with increasing B/C (Fig. 2E) (24). For comparison, for a helical spring with a circular cross-section made of an isotropic material, $B/C = 1 + \nu$, with Poisson ratio ν normally in the range $0 < \nu \lesssim 0.5$ so that typical springs exhibit minimal overwinding.

The observation of overwinding in fiber ribbons naturally leads to the question of whether entire tendrils also overwind. Whereas both young and old fiber ribbons always overwind, recently coiled, fully hydrated tendrils ("young" tendrils) do not overwind, but mature, dry tendrils ("old" tendrils) exhibit substantial overwinding (Fig. 2F and movies S9 and S10), and intermediate tendrils were variable in their overwinding behavior. The overwinding observed in old tendrils is likely due to the fact that as the tendril dries, the epidermal cells lose volume, and the tendril flattens down to a ribbon like shape similar to the internal fiber ribbon, so that $B/C > 1$.

To investigate the mechanical and functional consequences of overwinding, we measured the force required to axially stretch tendrils using a custom force measurement setup (20). Force-extension curves measured for a total of 20 tendrils show a variety of mechanical responses; in Fig. 3, we plot the dimensionless force $\tilde{F}$ against the scaled displacement Δl (detailed definitions of Δl and $\tilde{F}$ are in the supplementary text) for the two most extreme cases, a young tendril (red) and an old tendril (blue). For each, we show the results for a segment containing the perversion (Fig. 3; dotted curves indicate "perverted"), and another for a segment without it (Fig. 3; solid curves indicate "clamped"). In the young tendril, the perverted segment is always softer than the clamped segment (Fig. 3A). In contrast, the perverted segment of the old tendril is initially softer than the clamped segment but becomes stiffer at large extensions. Plotting the difference $\Delta f = f(\text{perverted}) - f(\text{clamped})$, where the scaled force f is obtained by dividing each force curve by its own initial slope (Fig. 3B), we see that for the young tendril in which no overwinding occurs, Δf is always negative, indicating that the perversion consistently decreases the force necessary to stretch the tendril relative to the clamped case. However, in the old, overwinding tendril the perversion actually increases the force needed to stretch the tendril as Δl increases.

To quantify the behaviors bounded by these two extreme tendril measurements, we also calculated force-extension curves using our mathematical models. The dimensionless force-extension curves for filaments with $B/C = 1/5$ (red), 1 (green), and 5 (blue) are shown in Fig. 3C. Similar to the behavior of the young tendril, in the filament with $B/C = 1/5$ (no overwinding), the presence of the perversion decreases the stiffness of the system—the force needed to axially extend the filament. However, the force response qualitatively changes when $B/C \gtrsim 3$, and the filament exhibits substantial overwinding. As in the old tendril, initially the perversion decreases the force needed to stretch the filament, but at large extensions, the perversion actually increases the force needed; the differential stiffness of the system is non-monotonic. Indeed, we observed that the difference $\Delta\tilde{F} = \tilde{F}(\text{perverted}) - \tilde{F}(\text{clamped})$ is always negative for filaments with $B < C$, whereas in overwinding filaments with large B/C values, $\Delta\tilde{F}$ transitions to positive values at large extensions (Fig. 3D). Thus, in overwinding filaments a helical perversion initially softens the force response but eventually stiffens the filament relative to the clamped case, which is a behavior qualitatively different from earlier theoretical studies (6, 16), in which overwinding was not observed in the range of B/C values studied. The difference in scaled force Δf shown in the Fig. 3D inset is consistent with experimental observations (Fig. 3B), indicating that the unusual force-extension behavior shown in Fig. 3D explains the extremes observed in the two tendrils.

Collectively, our observations raise questions at an evolutionary level about the ubiquity of this mechanism in other tendril-bearing species and at a mechanical level about the functional principles of these soft twistless springs. Preliminary studies of Passiflora tendrils reveal a band of g-fibers, suggesting a similar coiling mechanism (fig. S5); however, both young and old coiled Passiflora tendrils exhibit overwinding (fig. S5 and movie S11). Although Cucurbitaceae and Passifloraceae are from the same phylogenetic clade, their tendrils have evolved independently (25), inviting future comparative studies between species as well as investigations of subcellular processes regulating asymmetric contraction. Functionally, the combination of mechanical asymmetry, helical perversions, and large ratios of bending to twisting stiffness creates an autoadaptive springy tendril, one that is initially soft because it can overwind and then stiffens strongly when deformed further. Darwin himself wrote that "the tendril strikes some object, and quickly curls round ... contracts into a spire, dragging up the stem, and forming an excellent spring" (3). Our study illuminates and quantifies this proposal biophysically while suggesting biomimetic variants of the humble helical spring.

References and Notes

1. A. Gray, *Structural Botany: or Organography on the Basis of Morphology; To Which Is Added the Principles of Taxonomy and Phytography, and a Glossary of Botanical Terms* (Ivison, Blakeman, Taylor, New York, 1880).
2. H. v. Mohl, *Principles of the Anatomy and Physiology of the Vegetable Cell* (John Van Voorst, London, 1852).
3. C. Darwin, *On the Movements and Habits of Climbing Plants* (John Murray, London, 1865).
4. R. Dastur, G. Kapadia, *Ann. Bot. (London)* **45**, 279 (1931).
5. M. Jaffe, A. Galston, *Annu. Rev. Plant Physiol.* **19**, 417 (1968).
6. A. Goriely, M. Tabor, *Phys. Rev. Lett.* **80**, 1564 (1998).
7. H. Lisk, *Bot. Gaz.* **78**, 85 (1924).
8. D. T. MacDougal, *Annal. Bot.* **os-10**, 373 (1896).
9. S. Isnard, W. K. Silk, *Am. J. Bot.* **96**, 1205 (2009).
10. B. F. Wilson, R. R. Archer, *Annu. Rev. Plant Physiol.* **28**, 23 (1977).
11. W. Silk, R. Erickson, *Am. J. Bot.* **65**, 310 (1978).
12. J. L. Scher, N. M. Holbrook, W. K. Silk, *Planta* **213**, 192 (2001).
13. S. Isnard, A. R. Cobb, N. M. Holbrook, M. Zwieniecki, J. Dumais, *Proc. Biol. Sci.* **276**, 2643 (2009).
14. U. Nath, B. C. W. Crawford, R. Carpenter, E. Coen, *Science* **299**, 1404 (2003).
15. J. B. Keller, *Lect. Math Life Sci.* **13**, 257 (1980).
16. T. McMillen, A. Goriely, *J. Nonlinear Sci.* **12**, 241 (2002).
17. C. G. Meloche, J. P. Knox, K. C. Vaughn, *Planta* **225**, 485 (2007).
18. A. J. Bowling, K. C. Vaughn, *Am. J. Bot.* **96**, 719 (2009).
19. L. Goswami et al., *Plant J.* **56**, 531 (2008).
20. Materials and methods are available as supplementary materials on *Science* Online.
21. Z. Chen, C. Majidi, D. J. Srolovitz, M. Haataja, *Appl. Phys. Lett.* **98**, 011906 (2011).
22. S. Armon, E. Efrati, R. Kupferman, E. Sharon, *Science* **333**, 1726 (2011).
23. T. Savin et al., *Nature* **476**, 57 (2011).
24. A. Love, *A Treatise on the Mathematical Theory of Elasticity* (Courier Dover Publications, Mineola, NY, 1944).
25. P. F. Stevens, Angiosperm phylogeny Web site, www.mobot.org/MOBOT/Research/APweb/welcome.html (2008).

A Single Progenitor Population Switches Behavior to Maintain and Repair Esophageal Epithelium

David P. Doupé,[1,4]* Maria P. Alcolea,[1]* Amit Roshan,[1] Gen Zhang,[2] Allon M. Klein,[2,3] Benjamin D. Simons,[2,4] Philip H. Jones[1]†

Diseases of the esophageal epithelium (EE), such as reflux esophagitis and cancer, are rising in incidence. Despite this, the cellular behaviors underlying EE homeostasis and repair remain controversial. Here, we show that in mice, EE is maintained by a single population of cells that divide stochastically to generate proliferating and differentiating daughters with equal probability. In response to challenge with all-trans retinoic acid (atRA), the balance of daughter cell fate is unaltered, but the rate of cell division increases. However, after wounding, cells reversibly switch to producing an excess of proliferating daughters until the wound has closed. Such fate-switching enables a single progenitor population to both maintain and repair tissue without the need for a "reserve" slow-cycling stem cell pool.
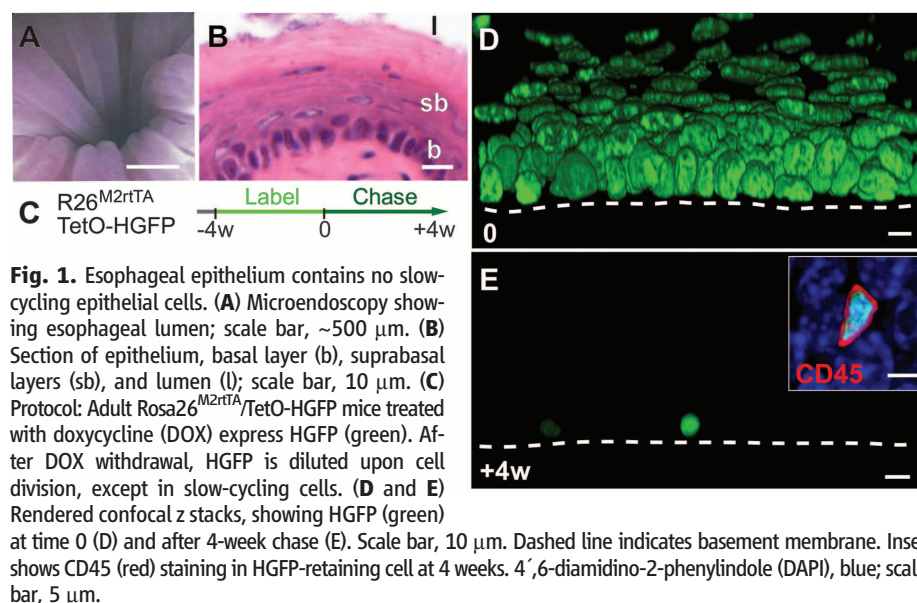
Murine esophageal epithelium (EE) consists of layers of keratinocytes. This tissue lacks structures such as crypts or glands that form stem cell niches in other epithelia (Fig. 1, A and B) (1–5). Proliferation is confined to cells in the basal layer (6). On commitment to terminal differentiation, basal cells exit the cell cycle and subsequently migrate to the tissue surface from which they are shed. Early studies suggested that all proliferating cells were functionally equivalent, but recent reports propose that a discrete population of slow-cycling stem cells is responsible for both maintenance and wound healing (7–11). This controversy and the importance of EE in disease motivated us to resolve the proliferative cell behavior in homeostatic EE and in tissue challenged by systemic treatment with the vitamin A metabolite all-trans retinoic acid (atRA) or acute local wounding (12, 13).

To investigate cell division rates in EE, we used a transgenic label-retaining cell (LRC) assay (Fig. 1C) (1, 14, 15). Doxycycline (DOX) induction of the fusion protein Histone-2B enhanced green fluorescent protein (HGFP) expression in

Rosa26[M2rtTA]/TetO-HGFP mice resulted in nuclear fluorescent labeling throughout the EE (Fig. 1D and fig. S1A). When DOX is withdrawn, HGFP is diluted by cell division, leaving 0.4% basal layer cells (561 out of 140,000) retaining label after a 4-week chase (Fig. 1E and fig. S1B). Three-dimensional imaging showed that these LRCs had smaller nuclei than the surrounding keratinocytes and did not stain for the basal keratinocyte marker Keratin14 (0 out of 561 LRCs) (fig. S1, C and D). The stem cell markers CD34

and *Lgr5* were also undetectable in LRCs or other cells (figs. S2 and S3) (2, 4, 10, 16). However, 99.9% (2457 out of 2459) of LRCs were positive for the pan leukocyte marker CD45 (Fig. 1E, inset), comprising a mixture of Langerhans cells and lymphocytes (fig. S1, E and F). These findings lead to the unexpected conclusion that, unlike tissues such as the epidermis, there are no slow-cycling or quiescent epithelial stem cells in EE (1, 17). Indeed, HGFP dilution in basal cells was strikingly homogeneous, suggesting that all cells divide at a similar rate of about twice per week (fig. S1G).

Although epithelial cells have the same rate of division, they may still differ in their ability to generate cycling and differentiated progeny. We therefore used inducible cre-lox–based genetic marking to investigate whether the proliferating cell population is heterogeneous and to quantify cell behavior (18, 19). The fate of single-cell-derived clones was tracked in cohorts of adult Ahcre[ERT] R26[flEYFP/wt] mice at multiple time points over a year after induction, during which period EE was homeostatic (Fig. 2A and fig. S4). Crucially, analysis of the composition of clones at 1 year showed that they were representative of unlabeled cells (fig. S5). Over the time course, clone number decreased through differentiation, whereas the size of the remaining clones progressively increased (Fig. 2, B and C). Although variation in labeling efficiency limits the accuracy with which the proportion of labeled cells can be estimated, within statistical error,

[1]Medical Research Council (MRC) Cancer Cell Unit, Hutchison-MRC Research Centre, Cambridge CB2 0XZ, UK. [2]Cavendish Laboratory, Department of Physics, J. J. Thomson Avenue, University of Cambridge, Cambridge CB3 0HE, UK. [3]Department of Systems Biology, Harvard Medical School, 200 Longwood Avenue, Boston, MA 02115, USA. [4]The Wellcome Trust/Cancer Research UK Gurdon Institute, University of Cambridge, Tennis Court Road, Cambridge CB2 1QN, UK.

*These authors contributed equally to this work.
†To whom correspondence should be addressed. E-mail: phj20@cam.ac.uk

Fig. 1. Esophageal epithelium contains no slow-cycling epithelial cells. (**A**) Microendoscopy showing esophageal lumen; scale bar, ~500 μm. (**B**) Section of epithelium, basal layer (b), suprabasal layers (sb), and lumen (l); scale bar, 10 μm. (**C**) Protocol: Adult Rosa26[M2rtTA]/TetO-HGFP mice treated with doxycycline (DOX) express HGFP (green). After DOX withdrawal, HGFP is diluted upon cell division, except in slow-cycling cells. (**D** and **E**) Rendered confocal z stacks, showing HGFP (green) at time 0 (D) and after 4-week chase (E). Scale bar, 10 μm. Dashed line indicates basement membrane. Inset shows CD45 (red) staining in HGFP-retaining cell at 4 weeks. 4´,6-diamidino-2-phenylindole (DAPI), blue; scale bar, 5 μm.

Supplementary Material for

How the Cucumber Tendril Coils and Overwinds

Sharon J. Gerbode, Joshua R. Puzey, Andrew G. McCormick, L. Mahadevan*

*To whom correspondence should be addressed. E-mail: lm@seas.harvard.edu

This PDF file includes:

Materials and Methods

Supplementary Text

Figs. S1 to S5

References (*26–29*)

Other Supplementary Material for this manuscript includes the following:
(available at www.sciencemag.org/cgi/content/full/337/6098/1087/DC1)

Movies S1 to S11

Section 1: Materials and Methods

Description of growth conditions

All plants were grown in the Department of Organismic and Evolutionary Biology greenhouses at Harvard University in long day conditions of 16 hour light/8 hour dark at a constant temperature of approximately 25°C.

Microscopy

A Zeiss AxioImager Z2 (Harvard Imaging Center) fitted with a Zeiss AxioCam Mrc digital camera was used for capturing darkfield and UV images of tendril cross sections. Fiber ribbons were imaged with an Insight Spot camera mounted on a Leica Wild M10 dissecting scope. Color images of tendrils, models, and fiber ribbons were taken with a Nikon D40x.

Fiber ribbon extraction

To extract fiber ribbons from whole tendrils, a solution of 2% Driselase (by weight) in phosphate buffered saline (PBS) was prepared. Since Driselase does not go completely into solution in PBS, the mixture was vortexed vigorously and then allowed to sit for 30 minutes. A fresh tendril was submerged in the Driselase supernatant and stored at 37°C overnight. After soaking overnight, the tendril was removed and briefly rinsed in fresh PBS. Forceps were used to gently slide the broken-down epidermal cells off of the fiber ribbon.

Physical model construction

Composite bilayer strips were constructed from prestrained silicone rubber in a three step process. First, a wide silicone rubber sheet was stretched along one axis to approximately 1.75 times its initial length (strain = 1.75), and was held clamped at this length. Second, another silicone layer consisting of Dow-Corning 732 multipurpose silicone sealant was added to the

stretched sheet along the strained axis, far from the edges of the sheet. Upon curing, the two layers were permanently bonded, creating a composite prestrained structure. In the final step, strips approximately 8 mm wide were cut along the stretched direction, and then the ends of the strips were released, allowing the composite material to relax to its equilibrium shape, with intrinsic curvature set by the relative strain, thickness, and stiffness of the two layers.

Force measurement apparatus

Tendrils were clamped at one end to a translation stage (Newport 426 crossed-roller bearing linear stage, with a Newport universal controller, model ESP 300) and clamped at the other end to a full bridge thin beam load cell (Omega LCL-113G) connected via a digital transmitter (Omegabus D1521) to RS-232. Custom LabVIEW software was used to move the translation stage in steps of 0.1 mm, measure force with the load cell, and simultaneously image the tendril with a digital ccd camera (Allied Vision Technologies Marlin) to monitor overwinding or unwinding behavior. Since both ends of the tendril were clamped, the ends were prevented from rotating during extension.

Numerical simulations of helical rods

As described in the main text, tendrils are a composite of a soft, fleshy bulk and a very stiff fiber ribbon. Here, we do not analyze the detailed mechanics of the composite tendril, and instead focus on a simple model that allows us to uncover the mechanical response of the tendril using a 1-dimensional equivalent filament with a naturally helical shape due to the asymmetric shrinkage of the fiber ribbon. This approximation allows us to capture the mechanics of the tendril on length scales that are large compared to its radius, as well as its bending, twisting, shear and extensional stiffness which we assume to be uniform along the filament. As the filament deforms in response to boundary or body forces, there is an elastic potential energy associated

3

with bending, twisting, shear and extensional deformations as well as a kinetic energy associated with the velocity of the rod (although the effect of inertia is irrelevant in our problem, as expected). Geometrically, the deformed rod is described by a curvature vector $\mathbf{k} - \mathbf{k}_0$ which describes how a material frame attached to a cross-section bends and twists relative to its intrinsic curvature $\mathbf{k}_0$, a local shear vector $\sigma - \sigma_0$ that describes the axial extension and planar shear relative to the intrinsic shear σ_0, a local centerline velocity $\mathbf{v}$, and a local angular velocity $\mathbf{w}$. The total energy of the rod is then given by (*28*):

$$
\begin{aligned}
E_{bend/twist} &= \frac{1}{2} \int_0^S (\mathbf{k} - \mathbf{k}_0)^T \mathbf{B} (\mathbf{k} - \mathbf{k}_0) \, ds \\
E_{stretch/shear} &= \frac{1}{2} \int_0^S (\sigma - \sigma_0)^T \mathbf{G} (\sigma - \sigma_0) \, ds \\
E_{translate} &= \frac{1}{2} \int_0^S \rho \mathbf{v}^T \mathbf{v} \, ds \\
E_{rotate} &= \frac{1}{2} \int_0^S \mathbf{w}^T \mathbf{I} \mathbf{w} \, ds
\end{aligned}
\tag{1}
$$

where we have assumed a simple quadratic form for the potential energy terms and where S is the total length of the rod, $\mathbf{B}$ is the local bending/twisting stiffness matrix, $\mathbf{G}$ is the local shearing/stretching stiffness matrix, ρ is the mass per unit length, and $\mathbf{I}$ is the moment of inertia of the cross-section. Our model used is similar, but not identical, to that described in (*27*); in particular, we differ by accounting for the role of both extensional and shear deformations; a complete description of this generalized theory will follow in a future paper. Although the Hamiltonian above is quadratic, the resulting Euler-Lagrange equations are nonlinear owing to the fact that we make no approximations in describing the curvature and torsion of the centerline of the filament, both of which can be relatively large.

To make progress in solving for the shape of the composite filament, we discretize the energy 1, describing the rod's centerline by n+1 vertices connected by n edges, so that we can derive a discrete set of equations of motion for the vertices by using standard techniques from

the calculus of variations. The equations of motion are then integrated using a semi-implicit Euler method, and the boundary conditions are explicitly applied at each time step. Since our experiments were carried out quasi-statically, the effects of inertia were negligible so that we used an over damped version of the equations of motion, as $\rho v^2/Bk^2 \ll 1, I\omega^2/Bk^2 \ll 1$. Furthermore, our filaments were very stiff in shear and extension so that we took $B/\sigma L^2 \ll 1$. To mimic the aging of the tendril, we varied the ratio of the bending to twisting stiffness.

The mechanical response of a tendril with a perversion may be understood by first constructing one. We clamp a naturally curved right handed helix to its mirror image, a left handed helix; the internal clamping point chosen to have no intrinsic curvature. Next, the ends of the rod were clamped (and unable to rotate) to supports that were pulled apart at a constant, quasi-static velocity. This system has a natural symmetry about the perversion that effectively reduces the problem into deforming a single helix with the mid-point being free to rotate but unable to translate in the axial direction. Thus, the mathematical significance of a perversion is that it changes the effective boundary conditions for each of its constituent helices by allowing them to rotate about their point of chiral asymmetry and accommodate the applied deformations by either overwinding or or unwinding depending on the ratio of the bending to twisting stiffness of the filament.

Dimensionless force-extension curves

To compare between tendrils of different lengths and stiffnesses, and also to enable comparison with our numerical simulations, we scaled the measured force-extension curves by defining the scaled displacement $\Delta l = (L - L_0)/S$ as the instantaneous axial length L of the tendril relative to its relaxed axial length L_0, divided by its total arc length S. Additionally, we defined the dimensionless force $\tilde{F}$ as the force F measured for any given tendril or numerical simulation, divided by an arbitrary force constant F_0. We chose F_0 to be the force required to initially

deform the perverted segment of the young tendril (dotted red curve in Fig. 3A) by a unit scaled displacement, i.e. $F_0 = \partial F / \partial (\Delta l)$ of the force-extension curve of the perverted segment of the young tendril.

Section 2: Theory

Intrinsic curvature of a prestrained bilayer ribbon

In cucumber tendrils, we observe that coiling occurs as a result of the morphosis of the fiber ribbon, a bilayer strip of long cells that extends along the entire length of the tendril. As one layer of the ribbon shrinks relative to the other, the composite ribbon develops intrinsic curvature. We have experimentally mimicked this process using prestrained bilayer rubber models as described in the manuscript. Here we give expressions for the intrinsic curvature k_0 of a bilayer rectangular cross-section ribbon with prestrain induced by the differential shrinkage of the constituent strips using expressions derived for the curvature of a heated bimetallic strip that bends due to the differential expansion of its constituent elements by Timoshenko (*29*), which we include here for completeness.

Consider two elastic ribbons of equal width t and heights h_1 (lower red in Fig. S3) and h_2 (upper blue in Fig. S3) that are combined to make a bilayer ribbon. The lower layer has Young's modulus E_1 while the upper layer has Young's modulus E_2. The lower layer is first stretched to a strain value of ϵ_1^* and is held in tension. The upper layer is not stretched, so that $\epsilon_2^* = 0$, and is permanently bonded to the lower layer. Then, when tension is released on the bonded bilayer ribbon, it relaxes to its equilibrium configuration with strains ϵ_1 and ϵ_2 and curvature k_0. The value of the intrinsic curvature k_0 is determined by the relative strain, Young's moduli, and heights of each layer. Both force and torque are balanced in the bilayer ribbon when it is left

6

free, so that

$$F_1 = F_2 \quad \text{(Force balance)}$$

$$F_1 h_1/2 + F_2 h_2/2 = k_0(E_1 I_1 + E_2 I_2) \quad \text{(Torque balance)}$$

where $I_1 = (\frac{th_1^3}{12})$ and $I_2 = (\frac{th_2^3}{12})$ are, respectively, the moment of area of the lower and upper layers, and $F_1 = \epsilon_1 E_1 h_1 t$ and $F_2 = \epsilon_2 E_2 h_2 t$ are the forces in each layer. Finally, on the interface where the layers are glued together, the total strain must be equal so that

$$\epsilon_1^* + F_1/E_1 h_1 t + k_0 h_1/2 = k_0 h_2/2 + F_2/E_2 h_2 t + \epsilon_2^*$$

Solving the above system of equations for $\epsilon_1, \epsilon_2, k_0$ yields (29)

$$k_0 = \frac{6(\epsilon_2^* - \epsilon_1^*)(1+m)^2}{(h_1 + h_2)(3(1+m)^2 + (1+mn)(m^2 + \frac{1}{mn}))} \tag{2}$$

where $m = h_1/h_2$ and $n = E_1/E_2$. We see that the curvature is proportional to the difference in the strain between the two strips and inversely proportional to the thickness of the composite.

Overwinding in the limit of infinite bending stiffness

Overwinding behavior can be intuitively understood in the limit of infinite bending stiffness relative to twisting stiffness by considering the simple case of a single helix with N turns, pitch p and radius r (Fig. S4A). This helix has uniform curvature k_0 and twist w_0 given by

$$k_0 = \frac{r}{(r^2 + (p/2\pi)^2)}$$

$$w_0 = \frac{p/2\pi}{(r^2 + (p/2\pi)^2)}$$

The arclength S of this helix is related to the pitch, radius, and number of turns by $S = N\sqrt{(2\pi r)^2 + p^2}$ and its axial length L is given by $L = Np$. If this initial helix is slightly

deformed to increase its axial length from L to $L + \delta L$ without increasing its total arclength S (ie. without stretching), we assume that it will take on a new helical shape with new pitch $p + \delta p$, radius $r + \delta r$, and number of turns $N + \delta N$. If the number of helical turns is held fixed by extending the helix with both ends clamped, then $\delta N = 0$. In this case, the axial deformation δL can be accommodated by changing the pitch and radius to reduce the curvature to $k_0 - \delta k$, ie. by flattening out the helix (Fig. S4B).

However, in the limit of infinite bending stiffness relative to twisting stiffness, the helix curvature cannot change, so $\delta k = 0$. In this case, the axial deformation δL can still be achieved by allowing one end of the helix to rotate, increasing the number of turns by δN. In this case, the pitch and radius both change so as to maintain constant curvature k_0, and the number of turns increases correspondingly in order to accommodate the total helix arclength S given the new pitch and radius (Fig. S4C). This increase in the number of turns is precisely what occurs in the experimentally observed overwinding.

Condition for overwinding in a composite rod with finite bending stiffness

For helical filaments with finite bending and twisting stiffness, the effect of overwinding can again be predicted for the simple case of a single helix, following Love (*24*), which we include here for completeness.

Again we consider an initial helix with pitch p, radius r, and arclength S, but now the helix has finite bending stiffness B and twisting stiffness C. A helix with pitch p and radius r is equivalently defined by its pitch angle $\alpha = \arctan(p/2\pi r)$, shown in Fig. S4. In terms of this pitch angle and the arclength, the axial length of the helix is $L = S\sin(\alpha)$. The helix can be

described in cylindrical coordinates as

$$r(s) = r$$

$$\theta(s) = s\cos(\alpha)/r$$

$$z(s) = s\sin(\alpha)$$

Here the radial coordinate is a constant r, the angular coordinate θ varies from 0 to $\vartheta = S\cos\alpha/r$ at the other end, the vertical coordinate varies from 0 at one end to L at the other, and $N = \vartheta/2\pi$ is the total number of turns in the helix.

We now consider small deformations of the helix due to a force F and torque τ applied at both ends. In response to these, the helix will take on a new equilibrium shape, which we assume is a helix with the same arclength S, but new pitch angle $\alpha + \delta\alpha$ and radius $r + \delta r$. The new shape is determined by the equations of mechanical equilibrium for force and torque:

$$F = \frac{1}{Sr^2}\left[\delta L(C\cos^2\alpha + B\sin^2\alpha) + 2\pi r\,\delta N(C - B)\sin\alpha\cos\alpha\right]$$

$$\tau = \frac{1}{Sr}\left[\delta L(C - B)\sin\alpha\cos\alpha + 2\pi r\,\delta N(C\sin^2\alpha + B\cos^2\alpha)\right]$$

where δN is the change in the total number of turns. Negative δN indicates unwinding, while positive δN corresponds to overwinding. In order to determine whether overwinding occurs when the helix is extended to length $L + \delta L$ under only an applied axial force, we set the applied torque $\tau = 0$ and solve for δN and δL in terms of F, l, r, B, and C. With two equations and two unknowns, we obtain the relations given in (*24*):

$$\delta L = Sr^2(\frac{\sin^2\alpha}{B} + \frac{\cos^2\alpha}{C})F$$

$$\delta N = \frac{Sr}{2\pi}\sin\alpha\cos\alpha(\frac{1}{C} - \frac{1}{B})F$$

Since the helix pitch angle α is between 0 and $\pi/2$, the factor of $\sin\alpha\cos\alpha$ is always positive. Thus, this prediction for small deformations shows that the change in number of turns is positive

9

if the bending stiffness B is greater than the twisting stiffness C, and negative if $B < C$, consistent with our observations of overwinding in cucumber tendrils and numerical simulations. We note that since this linearized prediction assumes small changes in shape, it cannot quantitatively predict the eventual unwinding that is observed in the numerical simulations and the experiments. Nevertheless, this simple calculation correctly predicts the qualitative behavior observed for small extensions.

Section 3: Movie Captions

Movie S1: Time-lapse movies of tendril searching for a support and coiling

Movie S2: Drying and rehydrating a fiber ribbon

Movie S3: Drying and rehydrating a whole tendril

Movie S4: Unwinding of a physical model

Movie S5: Overwinding of a fiber ribbon

Movie S6: Overwinding in a physical model with ribbon on inside and wire on outside

Movie S7: Unwinding of a numerical filament

Movie S8: Overwinding of a numerical filament

Movie S9: Unwinding of a young cucumber tendril

Movie S10: Overwinding of an old cucumber tendril

Movie S11: Overwinding of a passiflora tendril

Figure S1: **Tendril climbing via helical coiling.** Cross-hairs mark the initial position of the shoot apex and highlight how tendril coiling winches the plant upward toward the support. Top: The tip of the tendril initially wraps around and attaches to the supporting rod (Time = 0). Middle: A helical perversion (arrow) initiates in the suspended tendril (Time = 120 minutes). Bottom: The tendril shortens axially by coiling into a pair of helices with opposite handedness connected by a helical perversion (Time = 390 minutes).

Figure S2: **Extracted tendril fiber ribbon cut lengthwise.** The same fiber ribbon is progressively cut lengthwise to yield narrower and narrower strips that retained the original shape. Arrows indicate helical perversion in all panels. Left: The intact fiber ribbon. Middle: Resulting fiber ribbon from one lengthwise cut. Right: The fiber ribbon from the middle panel is cut lengthwise again, yielding an even narrower ribbon with the same shape.
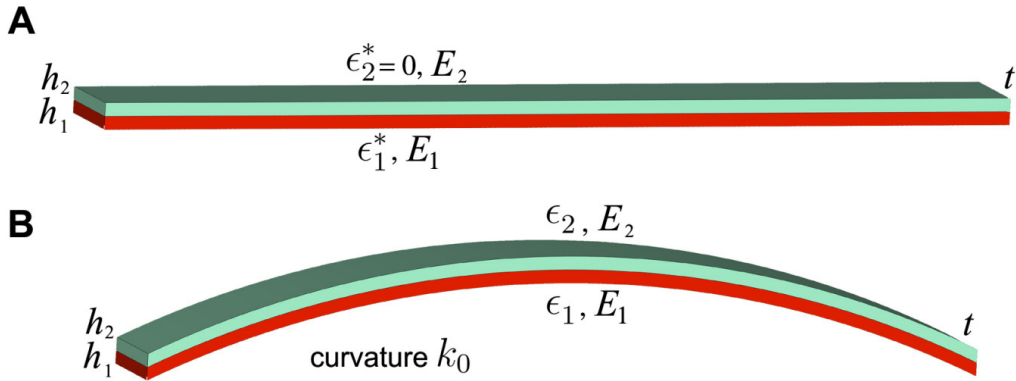

Figure S3: **Prestrain in a ribbon bilayer causes curvature.** (A) Two elastic ribbons of equal width t and heights h_1 (lower red) and h_2 (upper blue) are combined to make a bilayer ribbon. The lower layer is stretched to a strain value of ϵ_1^* and held in tension, while the upper layer is not stretched, so that $\epsilon_2^* = 0$. (B) When tension is released on the bilayer ribbon, it relaxes to its equilibrium configuration with strains ϵ_1 and ϵ_2 and curvature k_0.
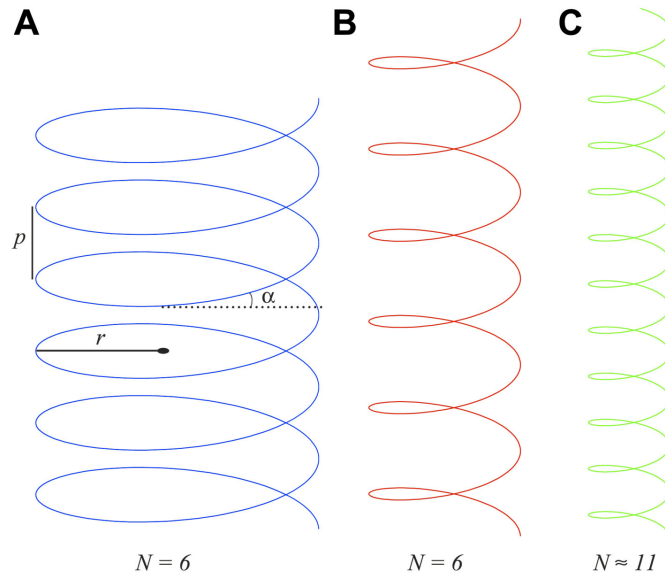
Figure S4: **Intuitive geometric explanation of overwinding in the limit of infinite bending stiffness.** (A) A helix with pitch p, radius r, pitch angle $\alpha = \arctan(p/2\pi r)$ and axial length L. (B) A deformed helix with increased axial length $L + \delta L$, achieved by maintaining a constant number of helical turns (ie. enforcing no unwinding or overwinding). (C) A deformed helix with increased axial length achieved in the limit of infinite bending stiffness by maintaining constant curvature k.
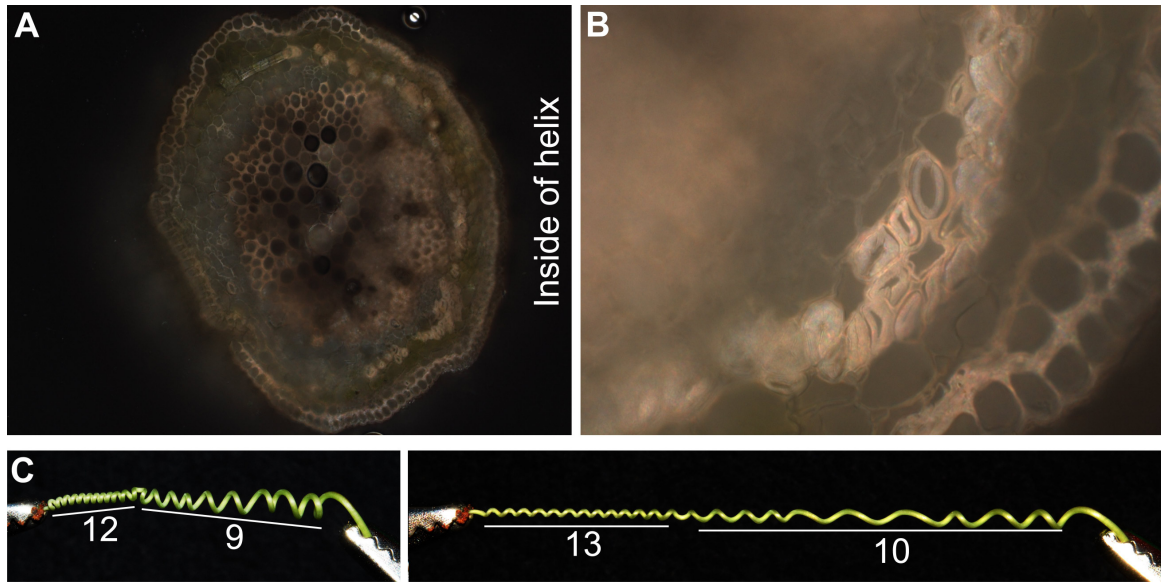
Figure S5: **Passiflora tendril anatomy and overwinding behavior.** (A) Cross section of coiled *Passiflora sp.* tendril. Gelatinous fiber (g-fiber) cells are present on the ventral side of the tendril, ie. on the inside of the helix. (B) Magnified view of g-fiber cells. Artifactual detachment of the gelatinous fiber from the secondary wall, as seen in panel B has been shown to be a distinctive characteristic of g-fiber cells (*17, 26*). (C) A coiled *Passiflora sp.* is shown in its relaxed configuration. When tension is applied, the tendril overwinds and adds additional turns on both sides of the helical perversion.

References and Notes

1. A. Gray, *Structural Botany: or Organography on the Basis of Morphology; To Which Is Added the Principles of Taxonomy and Phytography, and a Glossary of Botanical Terms* (Ivison, Blakeman, Taylor, New York, 1880).

2. H. v. Mohl, *Principles of the Anatomy and Physiology of the Vegetable Cell* (John Van Voorst, London, 1852).

3. C. Darwin, *On the Movements and Habits of Climbing Plants* (John Murray, London, 1865).

4. R. Dastur, G. Kapadia, *Ann. Bot. (Lond.)* **45**, 279 (1931).

5. M. Jaffe, A. Galston, The physiology of tendrils. *Annu. Rev. Plant Physiol.* **19**, 417 (1968). doi:10.1146/annurev.pp.19.060168.002221

6. A. Goriely, M. Tabor, Spontaneous helix hand reversal and tendril perversion in climbing plants. *Phys. Rev. Lett.* **80**, 1564 (1998). doi:10.1103/PhysRevLett.80.1564

7. H. Lisk, Cellular structure of tendrils. *Bot. Gaz.* **78**, 85 (1924). doi:10.1086/333357

8. D. T. MacDougal, *Annal. Bot.* **os-10**, 373 (1896).

9. S. Isnard, W. K. Silk, Moving with climbing plants from Charles Darwin's time into the 21st century. *Am. J. Bot.* **96**, 1205 (2009). doi:10.3732/ajb.0900045 Medline

10. B. F. Wilson, R. R. Archer, Reaction wood: Induction and mechanical action. *Annu. Rev. Plant Physiol.* **28**, 23 (1977). doi:10.1146/annurev.pp.28.060177.000323

11. W. Silk, R. Erickson, Kinematics of hypocotyl curvature. *Am. J. Bot.* **65**, 310 (1978). doi:10.2307/2442271

12. J. L. Scher, N. M. Holbrook, W. K. Silk, Temporal and spatial patterns of twining force and lignification in stems of Ipomoea purpurea. *Planta* **213**, 192 (2001). doi:10.1007/s004250000503 Medline

13. S. Isnard, A. R. Cobb, N. M. Holbrook, M. Zwieniecki, J. Dumais, Tensioning the helix: A mechanism for force generation in twining plants. *Proc. Biol. Sci.* **276**, 2643 (2009). doi:10.1098/rspb.2009.0380 Medline

14. U. Nath, B. C. W. Crawford, R. Carpenter, E. Coen, Genetic control of surface curvature. *Science* **299**, 1404 (2003). doi:10.1126/science.1079354 Medline

15. J. B. Keller, *Lect. Math Life Sci.* **13**, 257 (1980).

16. T. McMillen, A. Goriely, Tendril perversion in intrinsically curved rods. *J. Nonlinear Sci.* **12**, 241 (2002). doi:10.1007/s00332-002-0493-1

17. C. G. Meloche, J. P. Knox, K. C. Vaughn, A cortical band of gelatinous fibers causes the coiling of redvine tendrils: A model based upon cytochemical and immunocytochemical studies. *Planta* **225**, 485 (2007). doi:10.1007/s00425-006-0363-4 Medline

18. A. J. Bowling, K. C. Vaughn, Gelatinous fibers are widespread in coiling tendrils and twining vines. *Am. J. Bot.* **96**, 719 (2009). doi:10.3732/ajb.0800373 Medline

19. L. Goswami *et al*., Stress generation in the tension wood of poplar is based on the lateral swelling power of the g-layer. *Plant J.* **56**, 531 (2008). [doi:10.1111/j.1365-313X.2008.03617.x](doi:10.1111/j.1365-313X.2008.03617.x) Medline

20. Materials and methods are available as supplementary materials on *Science* Online.

21. Z. Chen, C. Majidi, D. J. Srolovitz, M. Haataja, Tunable helical ribbons. *Appl. Phys. Lett.* **98**, 011906 (2011). [doi:10.1063/1.3530441](doi:10.1063/1.3530441)

22. S. Armon, E. Efrati, R. Kupferman, E. Sharon, Geometry and mechanics in the opening of chiral seed pods. *Science* **333**, 1726 (2011). doi:10.1126/science.1203874 Medline

23. T. Savin *et al*., On the growth and form of the gut. *Nature* **476**, 57 (2011). doi:10.1038/nature10277 Medline

24. A. Love, *A Treatise on the Mathematical Theory of Elasticity* (Courier Dover Publications, Mineola, NY, 1944).

25. P. F. Stevens, Angiosperm phylogeny website, www.mobot.org/MOBOT/Research/APweb/welcome.html (2008).

26. B. Clair, B. Thibaut, J. Sugiyama, On the detachment of the gelatinous layer in tension wood fiber. *J. Wood Sci.* **51**, 218 (2005). [doi:10.1007/s10086-004-0648-9](doi:10.1007/s10086-004-0648-9)

27. M. Bergou, M. Wardetzky, S. Robinson, B. Audoly, E. Grinspun, Discrete elastic rods. *ACM Trans. Graph.* **27**, 1 (2008). [doi:10.1145/1360612.1360662](doi:10.1145/1360612.1360662)

28. S. S. Antman, Nonlinear problems of elasticity (Springer, 2005), second edn.

29. S. Timoshenko, Analysis of bi-metal thermostats. *J. Opt. Soc. Am.* **11**, 233 (1925). doi:10.1364/JOSA.11.000233